

# 1 Modeled source apportionment of black carbon particles coated with a light-scattering shell

2  
3 Aki Virkkula

4 Finnish Meteorological Institute

5 Helsinki, Finland

## 6 7 **Abstract**

8 The Aethalometer model has been used widely for estimating the contributions of fossil fuel emissions  
9 and biomass burning to equivalent black carbon (eBC). The calculation is based on measured absorption  
10 Ångström exponents ( $\alpha_{\text{abs}}$ ). The interpretation of  $\alpha_{\text{abs}}$  is ambiguous since it is well-known that it not  
11 only depends on the dominant absorber but also on the size and internal structure of the particles, core  
12 size and shell thickness. In this work the uncertainties of the Aethalometer-model-derived apparent  
13 fractions of absorption by eBC from fossil fuel and biomass burning are evaluated with a core-shell Mie  
14 model. Biomass-burning fractions (BB(%)) were calculated for pure and coated single BC particles, for  
15 lognormal unimodal and bimodal size distributions of BC cores coated with ammonium sulfate, a  
16 scattering-only material. BB(%) was very seldom 0% even though BC was the only absorbing material in  
17 the simulations. The shape of size distribution plays an important role. Narrow size distributions result  
18 in higher  $\alpha_{\text{abs}}$  and BB(%) values than wide size distributions. The sensitivity of  $\alpha_{\text{abs}}$  and BB(%) to  
19 variations in shell volume fractions is the highest for accumulation mode particles. This is important  
20 because that is where the largest aerosol mass is. For the interpretation of absorption Ångström  
21 exponents it would be very good to measure BC size distributions and shell thicknesses together with  
22 the wavelength dependency of absorption.

## 23 24 **1. Introduction**

25 Incomplete combustion of organic fuels results in emission of light-absorbing carbon (LAC) particles  
26 that contain both black carbon (BC) and brown carbon (BrC). BrC is light-absorbing organic matter in  
27 atmospheric aerosols of various origins e.g., soil humics, humic-like substances (HULIS), tarry materials  
28 from combustion, bioaerosols (Andreae and Gelencser, 2006; Laskin et al., 2015). BrC can significantly  
29 absorb solar radiation in the ultraviolet–visible (uv–vis) wavelength range ( $\lambda \approx 300 - 800$  nm). The

1 radiative effects of BC and BrC vary in time during atmospheric aging. For many combustion sources  
2 the absorbance in fresh emission is almost completely caused by BC particles but during atmospheric  
3 transport they often get coated with some light-scattering compounds, for instance ammonium sulfate  
4 or light-absorbing organic carbon, BrC. For some sources (e.g. biomass burning) BrC may contribute  
5 substantially to light-absorption already in the directly emitted aerosols and either increase or decrease  
6 during aging. Thus, BrC is highly time-dependent as it's composition and absorption properties change  
7 during atmospheric oxidation processes (Laskin et al., 2015).

8

9 The absorption coefficient  $\sigma_{ap}$  is approximately proportional to the power function  $\lambda^{-\alpha_{abs}}$  where  $\lambda$  is  
10 the wavelength and  $\alpha_{abs}$  is the absorption Ångström exponent.  $\alpha_{abs}$  is generally used to distinguish  
11 aerosol types: for pure BC particles  $\alpha_{abs} \approx 1$  while other light absorbing aerosols (BrC, soil dust) it is  
12 clearly  $> 1$  (e.g., Kirchstetter et al., 2004; Bond and Bergstrom, 2006; Bergstrom et al., 2007; Moosmüller  
13 et al, 2011; Kirchstetter and Thatcher, 2012; Lack et al., 2012; Bond et al., 2013; Saleh et al., 2013; Laskin  
14 et al., 2015; Valenzuela et al., 2015; Devi et al., 2016). The method has been used not only for in situ  
15 absorption measurements but also for interpreting absorption coefficients retrieved from remote  
16 sensing measurements, such as the AERONET (e.g., Russell et al., 2010; Arola et al., 2011; [Chung et al.,](#)  
17 [2012](#); Cazorla et al., 2013; Feng et al., 2013; [Schuster et al., 2016](#); Wang et al., 2016).

18

19 One of the instruments used for measuring black carbon concentrations is the Aethalometer that  
20 collects aerosol on a filter tape, measures changes in light attenuation in the wavelength range of 370  
21 – 950 nm and calculates the equivalent black carbon (eBC) concentrations. The data are used also to  
22 calculate  $\alpha_{abs}$  and to estimate the contributions of fossil fuel emissions and biomass burning to eBC.  
23 The Aethalometer model (Sandradewi et al., 2008a) is probably the most widely-used method for this  
24 and it is even calculated automatically in the new Aethalometer model AE33. It is there assumed that  
25 the absorption Ångström exponents are  $\alpha_{ff} = 1$  and  $\alpha_{bb} = 2$  for eBC from fossil fuel and biomass burning,  
26 respectively. These are the default settings in the AE33, but also different  $\alpha_{ff}$  and  $\alpha_{bb}$  values have been  
27 used (Sandradewi et al., 2008b; Herich et al., 2011; Fuller et al., 2014; Harrison et al., 2013; Healy et al.,  
28 2017; Zotter et al., 2017; Helin et al., 2018).

29

1 The interpretation of  $\alpha_{\text{abs}}$  is ambiguous since it not only depends on the dominant absorber but also on  
2 the size and internal structure of the particles, core size and shell thickness. For instance, for pure BC  
3 particles,  $\alpha_{\text{abs}}$  may be  $< 1$  and BC particles coated with non-absorbing material may have  $\alpha_{\text{abs}}$  in the  
4 range from  $< 1$  to  $\sim 1.7$  (e.g., Gyawali et al., 2009; Lack and Cappa, 2010; Lack and Langridge, 2013; Liu  
5 et al., 2018; Chylek et al., 2019; Zhang et al., 2020). The present paper may be considered as an  
6 extension to the above-mentioned analyses since they did not explicitly analyze the effects on the  
7 Aethalometer model.

8  
9 The aim of this study is to estimate uncertainties of the Aethalometer-model-derived fractions of  
10 absorption by eBC from fossil fuel and biomass burning when spherical BC cores are coated by some  
11 non-absorbing material. **To state this more clearly, it is assumed that there is only one type of BC**  
12 **particles that can be called fossil fuel BC in the Aethalometer model terminology. Consequently, any**  
13 **deviations from biomass-burning fraction of BB% = 0 indicate uncertainty in the source appointment.**  
14 Biomass-burning fractions were calculated for pure and coated single particles, for lognormal unimodal  
15 and bimodal size distributions. The work is based on modeling only, no measurement data are used.

## 17 2. Methods

18 The BC cores were assumed to be coated with an ammonium sulfate shell by using two approaches. It  
19 was assumed 1) that the shell thickness the same for all particles in a size distribution (Fig. 1a) and 2)  
20 that the core volume fraction is the same for all particles in a size distribution (Fig. 1b). The core volume  
21 fraction was calculated from

$$22 \quad f_c = \frac{V_{\text{core}}}{V_p} = \left( \frac{D_{\text{core}}}{D_p} \right)^3 = \left( \frac{D_{\text{core}}}{D_{\text{core}} + 2s} \right)^3 \quad (1)$$

23 where  $V_p$  is the particle volume,  $V_{\text{core}}$  is the BC core volume,  $D_p$  is the particle diameter ( $= D_{\text{core}} + 2s$ ),  
24  $D_{\text{core}}$  is the core diameter and  $s$  the shell thickness. The shell volume fraction was then calculated  
25 from  $f_s = 1 - f_c$ . **The ratio of the coated particle diameter to the core diameter is an often used metric**  
26 **for presenting the coating of particles.  $R$ ,  $f_c$  and  $f_s$  can be calculated from each other as**

$$27 \quad R = \frac{D_p}{D_{\text{core}}} = \left( \frac{1}{f_c} \right)^{1/3} = \left( \frac{1}{1 - f_s} \right)^{1/3} \quad (2)$$

1 The number-weighted  $D_p$ -to- $D_{core}$  ratio is calculated from

$$2 \quad R_{N(D_p)} = \frac{\sum N_i R_i}{N_{tot}} = \frac{\sum N_i (D_{p,i} / D_{core,i})}{N_{tot}} \quad (3)$$

3 where  $N_i$  and  $R_i$  are the number concentration and  $D_p$ -to- $D_{core}$  ratio of the particle diameter  $D_{p,i}$ ,  
4 respectively. If  $f_s$  is independent of particle size – which is the assumption used in some of the  
5 simulations below – equation (3) simplifies to  $R_{N(D_p)} = R$ .

Formatted: Justified

6  
7 Lognormal size distributions  $n(D_p, D_g, \sigma_g)$  were generated where  $D_p$  is the particle diameter,  $D_g$  is the  
8 geometric mean diameter and  $\sigma_g$  the geometric standard deviation. The  $D_p$  range was 3 nm – 10  $\mu$ m.  
9 For the unimodal size distributions  $D_g$  range was 50 nm – 1  $\mu$ m and  $\sigma_g$  was given three values 1.4, 1.6,  
10 1.8 (Fig. 1c and 1d). Also bimodal size distributions were generated. For the small-particle mode the  
11 geometric mean diameter  $D_{g1}$  range was 50 – 100 nm, and the large-particle mode  $D_{g2}$  range was 100  
12 – 500 nm. In addition to varying the geometric mean diameters also the ratios of the number of particles  
13 in the two modes were varied. Two cases were used for this: 1)  $N_1 = 10N_2$ ,  $\sigma_{g1} = 1.4$ ,  $\sigma_{g2} = 1.6$  (Fig. 1e)  
14 and 2)  $N_1 = N_2$ ,  $\sigma_{g1} = 1.6$ ,  $\sigma_{g2} = 1.6$  (Fig. 1f).

15  
16 Absorption coefficients were calculated from

$$17 \quad \sigma_{ap}(\lambda) = \int Q_a(\lambda, D_p, m_{core}, m_{shell}, s) \frac{\pi}{4} D_p^2 n(D_p) dD_p \quad (4)$$

18 where  $Q_a$  is the absorption efficiency that is a function of the wavelength  $\lambda$ ,  $D_p$ , the complex refractive  
19 indices of the core and shell,  $m_{core}$  and  $m_{shell}$ , respectively, and the shell thickness  $s$ .  $Q_a$  was calculated  
20 using the N-Mie ~~fortran~~Fortran code that is based on a recursive algorithm of Wu and Wang (1991).  
21 The code calculates the extinction, scattering and absorption efficiency factors for n-layered spheres.  
22 The complex refractive indices were  $m_{core} = 1.85 + 0.71i$  (BC as in Lack and Cappa, 2010) and  $m_{shell} =$   
23  $1.52 + 0i$  (ammonium sulfate) for the core and shell, respectively. Absorption coefficients were  
24 calculated for the Aethalometer wavelengths  $\lambda = 470$  nm and 950 nm and  $\alpha_{abs}$  was calculated from

$$25 \quad \alpha_{abs} = - \frac{\ln(\sigma_{ap}(\lambda = 470nm) / \sigma_{ap}(\lambda = 950nm))}{\ln(470/950)} \quad (5)$$

26 The wavelengths 470 nm and 950 nm were used as they are used also in the AE33 automatic source  
27 apportionment. In analyses of aerosol optical depth data from the AERONET network  $\alpha_{abs}$  is often

Formatted: Justified

1 calculated for the wavelength pair 440 nm and 870 nm (Russell et al., 2010; Schuster et al., 2016). To  
 2 evaluate the applicability of the simulations of the present work to AERONET data analyses  $\sigma_{ap}$  was  
 3 calculated also for these wavelengths and the respective  $\alpha_{abs}$  was calculated from them. There are size-  
 4 dependent differences between  $\alpha_{abs}(470/950)$  and  $\alpha_{abs}(440/870)$  but they are not big, see the  
 5 supplement, Figs. S1 and S2, so it may safely be concluded that the results to be presented below are  
 6 valid also for the AERONET data.

8 For the absorption due to particles from wood burning or biomass burning Zotter et al. (2017) give  
 9 the equation

$$\sigma_{ap,bb}(\lambda_2) = \frac{\sigma_{ap}(\lambda_1) - \sigma_{ap}(\lambda_2) \left(\frac{\lambda_1}{\lambda_2}\right)^{-\alpha_{ff}}}{\left(\frac{\lambda_1}{\lambda_2}\right)^{-\alpha_{bb}} - \left(\frac{\lambda_1}{\lambda_2}\right)^{-\alpha_{ff}}} \cdot \sigma_{a,bb}(\lambda_2) = \frac{\sigma_a(\lambda_1) - \sigma_a(\lambda_2) \left(\frac{\lambda_1}{\lambda_2}\right)^{-\alpha_{ff}}}{\left(\frac{\lambda_1}{\lambda_2}\right)^{-\alpha_{bb}} - \left(\frac{\lambda_1}{\lambda_2}\right)^{-\alpha_{ff}}} \quad (64)$$

11 where  $\alpha_{ff}$  and  $\alpha_{bb}$  are the  $\alpha_{abs}$  of fossil fuel and biomass burning BC in the Aethalometer model. Noting  
 12 that  $\sigma_{ap}(\lambda_1) = \sigma_{ap}(\lambda_2) (\lambda_1/\lambda_2)^{-\alpha_{abs}}$   ~~$\sigma_a(\lambda_1) = \sigma_a(\lambda_2) (\lambda_1/\lambda_2)^{-\alpha_{abs}}$~~  the fraction of absorption due to biomass  
 13 burning is

$$BB(\%) = 100\% \frac{\sigma_{ap,bb}(\lambda_2)}{\sigma_{ap}(\lambda_2)} = 100\% \frac{\left(\frac{\lambda_1}{\lambda_2}\right)^{-\alpha_{abs}} - \left(\frac{\lambda_1}{\lambda_2}\right)^{-\alpha_{ff}}}{\left(\frac{\lambda_1}{\lambda_2}\right)^{-\alpha_{bb}} - \left(\frac{\lambda_1}{\lambda_2}\right)^{-\alpha_{ff}}}$$

$$BB(\%) = 100\% \frac{\sigma_{a,bb}(\lambda_2)}{\sigma_a(\lambda_2)} = 100\% \frac{\left(\frac{\lambda_1}{\lambda_2}\right)^{-\alpha_{abs}} - \left(\frac{\lambda_1}{\lambda_2}\right)^{-\alpha_{ff}}}{\left(\frac{\lambda_1}{\lambda_2}\right)^{-\alpha_{bb}} - \left(\frac{\lambda_1}{\lambda_2}\right)^{-\alpha_{ff}}} \quad (75)$$

16 so that BB% depends on the Ångström exponents  $\alpha_{abs}$ ,  $\alpha_{ff}$  and  $\alpha_{bb}$ . Two settings for the constants were  
 17 used, the one presented in the AE33 manual:  $\alpha_{ff} = 1$  and  $\alpha_{bb} = 2$ , and the one presented by Zotter et al.  
 18 (2017) :  $\alpha_{ff} = 0.9$  and  $\alpha_{bb} = 1.68$ .

### 3. Results and discussion

### 1 3.1 Single particles

2 The absorption Ångström exponent  $\alpha_{\text{abs}}$  and the fraction of biomass-burning BC for single coated  
3 particles are shown in Fig. 2. The dashed lines in Figs. 2a, 2c, and 2e show the core diameter  $D_{\text{core}}$  of  
4 particles that have the same diameter  $D_p$  at all shell thicknesses. In Figs. 2b, 2d and 2f the dashed lines  
5 show the particle diameter  $D_p$  and  $f_s$  of particles that have the same  $D_{\text{core}}$  at all shell volume fractions  
6  $f_s$  in the range  $f_s \leq 99\%$ . The dependence of  $\alpha_{\text{abs}}$  on core and shell is presented twice. This is apparently  
7 superfluous but they are visualizations that complement each other.

8

9 The first approach (Figs. 2a, 2c, and 2e) shows that when  $D_{\text{core}} < \sim 150$  nm and  $s > \sim 25 - 50$  nm ~~the~~  
10 absorption Ångström exponent  $\alpha_{\text{abs}} > 1.4$ . The respective BB fractions are larger than about 40% or 60%  
11 for the Aethalometer model parameters of  $\alpha_{\text{ff}} = 1$ ,  $\alpha_{\text{bb}} = 2$  (pair 1) and  $\alpha_{\text{ff}} = 0.9$ ,  $\alpha_{\text{bb}} = 1.68$  (pair 2),  
12 respectively. Fig. 2a also shows that for  $D_{\text{core}} < \sim 100$  nm there are two maxima of the  $\alpha_{\text{abs}}$  when the  
13 shell grows thicker. In the second maximum  $\alpha_{\text{abs}} > \sim 1.6$ . As a result the BB fractions would be  $> 60\%$   
14 and even  $> 100\%$  for the two Aethalometer model parameter pairs. When  $D_{\text{core}}$  is in the range of  $\sim 170$ -  
15  $200$  nm  $\alpha_{\text{abs}} \approx 1$  and  $\alpha_{\text{abs}}$  decreases with a growing  $s$ . For larger core diameters the absorption Ångström  
16 exponent is even smaller. When  $D_{\text{core}} > 200$  nm  $\alpha_{\text{abs}} < 1$ , and even negative for  $D_{\text{core}} > \sim 360$  nm. Further,  
17 when  $D_{\text{core}} > 200$  nm,  $\alpha_{\text{abs}}$  does not grow essentially at all as a function of  $s$ .

18

19 The visualization of  $\alpha_{\text{abs}}$  as a function of shell volume fraction  $f_s$  and particle full diameter  $D_p$  (Fig. 2b)  
20 shows some other features. When  $D_p < 50$  nm,  $\alpha_{\text{abs}}$  varies in the range of 1.0 - 1.1 and it does not depend  
21 on  $f_s$  but in the  $D_p$  range of about 100 – 300 nm  $\alpha_{\text{abs}}$  depends strongly on  $f_s$ . When  $D_p \approx 500$  nm  $\alpha_{\text{abs}} <$   
22  $1$  for almost all shell volume fractions, up to  $f_s \sim 99\%$ . For larger particles  $\alpha_{\text{abs}}$  is close to 0 at all shell  
23 volume fractions.

24

25 The visualization also shows that the  $\alpha_{\text{abs}}$  value of 1, usually considered as indication of BC, is not a  
26 result of an unambiguous  $D_{\text{core}}-s$  (Fig. 2a) or  $D_p-f_s$  (Fig. 2b) combination.

27

### 28 3.2 Unimodal BC core size distributions, same coating thickness for all sizes

1 For single particles  $\alpha_{\text{abs}}$  depends clearly both the core size and the shell thickness. However, in real  
2 atmospheric studies the wavelength dependency of absorption by particle size distributions are  
3 measured. Here these were first modeled by assuming that pure BC particle size distributions get  
4 coated with ammonium sulphate layers so that the shell thickness is independent of particle size as  
5 visualized in Fig. 1a. For example, the shell thickness on a 50 nm BC particle would be the same as on a  
6 200 nm particle which means the shell volume fractions are not the same. The BC core geometric mean  
7 diameter ( $D_{\text{g,core}}$ ) was varied from 50 to 200 nm at 10 nm intervals. The geometric standard deviations  
8 of the size distributions were  $\sigma_{\text{g}} = 1.4$ ,  $\sigma_{\text{g}} = 1.6$ , and  $\sigma_{\text{g}} = 1.8$  representing narrow, average and wide  
9 size distributions. The shell thickness  $s$  varied from 0 to 250 nm at 1 nm intervals. Absorption coefficient  
10 and subsequently  $\alpha_{\text{abs}}$  was calculated for the full size distribution 3 – 2500 nm.

11

12 The results are first shown as a function of  $D_{\text{g,core}}$  and shell thickness  $s$  for the three size distribution  
13 widths (Fig. 3). There are both similarities and differences compared with the corresponding  
14 relationships of single particles (Fig. 2). For example, for single particles  $\alpha_{\text{abs}} \approx 1$  at  $D_{\text{core}} \approx 180$  nm for  
15 shell ~~thinesses~~ thicknesses  $s \approx 0 - 70$  nm as shown by the almost vertical  $\alpha_{\text{abs}} = 1$  isoline in Fig. 2a  
16 whereas for the size distributions with  $\sigma_{\text{g,core}} > 1$  the respective isoline is a strong function of both  $s$   
17 and  $\sigma_{\text{g,core}}$  (Fig. 3a). At all widths of the size distribution  $\alpha_{\text{abs}}$  increases with increasing shell thickness  
18 and then starts decreasing. For small core sizes ( $D_{\text{g,core}} < \sim 80$  nm)  $\alpha_{\text{abs}}$  has also a second maximum when  
19 the size distribution is narrow. The width of the size distribution has a clear effect on the  $\alpha_{\text{abs}}$ : for all  
20 core sizes and shell thicknesses  $\alpha_{\text{abs}}$  decreases with increasing  $\sigma_{\text{g,core}}$ .

21

22 Both for single particles and size distributions the first maximum of  $\alpha_{\text{abs}}$  is the smaller the larger the  
23  $D_{\text{g,core}}$  and  $\sigma_{\text{g,core}}$  are (Fig. 4a). The first maximum is reached at shell thickness  $s \approx 70 \pm 5$  nm for all size  
24 distribution widths although for single particles the variability of the shell thickness corresponding to  
25 the first maximum is larger (Fig. 4b). The first maximum  $\alpha_{\text{abs}}$  results in apparent BB fractions of up to  
26  $\sim 100\%$  for single particles and in the range from 0 to  $\sim 80\%$  for the size distributions and again the BB(%)  
27 is the smaller the larger the  $D_{\text{g,core}}$  and  $\sigma_{\text{g}}$  are (Fig. 4c and d).

28

1 This approach is further followed by plotting the parameters as a function of shell thickness for three  
 2 different BC core diameters, 50 nm, 70 nm, and 90 nm of single particles and core size distributions  
 3 with the geometric standard deviations of  $\sigma_{g,core} = 1.4, 1.6, \text{ and } 1.8$  (Fig. 5). This analysis can be  
 4 considered as a description of what may happen to the size distribution,  $\alpha_{abs}$  and the apparent BB(%)  
 5 during condensational growth on fresh small BC cores if the growing shell thickness were independent  
 6 of the core diameter, even if this is unrealistic. The shell volume fraction  $f_s$  increases to > 99.9% when  
 7 the shell thickness grows from  $s = 0$  nm to 250 nm on single 50 nm particles but to lower fractions for  
 8 the wider size distributions and larger core sizes so that for  $D_{g,core} = 90$  nm and  $\sigma_g = 1.8$   $f_s \approx 98\%$  even  
 9 with  $s = 250$  nm (Fig. 5a). The geometric mean diameter  $D_g$  of the whole size distribution grows to  $\sim 600$   
 10 nm when the shell thickness grows to 250 nm, minimal differences between the original widths (Fig.  
 11 5b). The width of the size distribution, i.e.,  $\sigma_g$  decreases fast to  $< 1.2$  (Fig. 4c). Such values correspond  
 12 to very narrow size distributions, not really observed in the real atmosphere.

13

14 The number-weighted  $D_p$ -to- $D_{core}$  ratio

15 ~~$$R_{N(D_p)} = \frac{\sum N_i R_i}{N_{tot}} = \frac{\sum N_i (D_{p,i} / D_{c,i})}{N_{tot}} \quad (6) \quad R_{N(D_p)}, \text{ Eq. (3)}$$~~

16 was calculated for the size range 90-600 nm to present the numbers comparable with papers that  
 17 present shell-to-core ratios of refractory BC (rBC) obtained from SP2 measurements. For instance,  
 18 Kondo et al. (2011) measured urban air of Tokyo and obtained the median  $R = 1.1$  with a range up to  
 19 about 1.3, the mean  $D_g = 64 \pm 6$  nm, and  $\sigma_g = 1.66 \pm 0.12$ . Moteki et al. (2007) conducted SP2  
 20 measurements in an aircraft in urban plumes on the Japanese coast. They fitted the data with lognormal  
 21 size distributions with mass median diameters (MMD) of 190 and 210 nm and  $\sigma_g$  of 1.55 and 1.45 for  
 22 fresh and aged rBC, respectively. The fresh rBC was thinly coated with  $R < 2$  and the aged rBC thickly  
 23 coated with  $R \sim 2$ . The MMD and  $\sigma_g$  values yield  $D_g = 107$  nm and 139 nm. Shiraiwa et al. (2008)  
 24 measured the mixing state and size distribution of BC aerosol with an SP2 at a remote island (Fukue) in  
 25 Japan. They observed that the BC number median diameters were in the range of 120–140 nm in every  
 26 air mass type and the median shell/core diameter ratio (R) in different air masses varied in the range of  
 27 1.2 – 1.6. However, they also observed that the fraction of R values in the range 2 – 3.5 was not  
 28 negligible either (Fig. 9 of Shiraiwa et al., 2008). Such values correspond to the range where  $\alpha_{abs}$  first

Formatted: Tab stops: Not at 3 cm + 16.5 cm



1 grows to  $>1.6$  for the narrow ( $\sigma_{g,core} = 1.4$ ) BC core size distribution that has the smallest geometric  
2 mean size ( $D_{g,core} = 50$  nm) but to lower values for the wider size distributions that have larger  $D_{g,core}$   
3 (Fig. 5c and 5d). The first maximum is reached at shell thicknesses of  $s \approx 70$  nm that corresponds to  $R \approx$   
4 2 and shell volume fractions of  $f_s \approx 90 \pm 8\%$  (Fig. 5b). Schwarz et al. (2008) reported statistics of rBC  
5 mass size distributions in urban aerosol:  $f_s = 9 \pm 6\%$ ,  $s = 20 \pm 10$  nm, MMD = 170 nm, and  $\sigma_g$  of 1.71  
6 which yields  $D_g = 72$  nm; in biomass burning emissions:  $f_s = 70 \pm 9\%$ ,  $s = 65 \pm 12$  nm, MMD = 210 nm,  
7  $\sigma_g = 1.43$  which yields  $D_g = 143$  nm and in background continental aerosol:  $f_s = 46 \pm 3\%$ ,  $s = 48 \pm 14$  nm,  
8 MMD = 210 nm, 1.55 which yields  $D_g = 118$  nm.

9  
10 The referenced studies show that the  $s$ ,  $R$ , and  $f_s$  values are in the range observed in ambient  
11 measurements studies. What is not realistic in atmospheric aerosol is the width of the size distribution,  
12 which soon decreases to  $\sigma_g < 1.2$  (Fig. 5c).

13  
14 After reaching the first maximum  $\alpha_{abs}$  decreases and for single particles and the narrowest core size  
15 distributions starts again growing and reaches a second maximum at shell thicknesses of  $s \approx 170$  nm  
16 that corresponds to  $R > 4$  and  $f_s > 98\%$ . Such  $s$  and  $R$  values are not in the range observed in the above-  
17 mentioned studies, nor are the low geometric standard deviations of  $\sigma_g < 1.1$  realistic so the second  
18 maximum can be considered as a theoretical value only. For size distributions with  $D_{g,core} > 70$  nm there  
19 is no second maximum  $\alpha_{abs}$ .

20  
21 As  $\alpha_{abs}$  increases and decreases it is clear that this applies to BB(%) as well (Fig. 5d-e). For the smallest  
22 core sizes ( $D_{g,core} = 50$  nm) and the narrowest size distributions ( $\sigma_{g,core} = 1.4$ ) the first maximum BB(%)  
23 may be as high as  $\sim 90\%$  when the values of  $\alpha_{ff} = 0.9$ ,  $\alpha_{bb} = 1.68$  are used in Eq. (57) but lower,  $\sim 50\%$   
24 when the values of  $\alpha_{ff} = 1$ ,  $\alpha_{bb} = 2$  are used. For the wider core size distributions the BB(%) fractions are  
25 lower. For the widest core size distributions ( $\sigma_{g,core} = 1.8$ ) clearly positive BB(%) values are reached only  
26 for the smallest core sizes.

27  
28 Fig. 5 can also be considered as a proxy for a time series of the development of  $\alpha_{abs}$  and derived BB(%)  
29 after emission of BC particles and their growth by condensation of nonabsorbing compounds. Similar

1 development –  $\alpha_{abs}$  increase to  $> 1.3$  and decrease to  $< 0.9$  during a several-day-long pollution episode  
2 during which the  $D_g$  of the whole size distribution grew possibly by condensation – was observed at  
3 SORPES in Nanjing, China (Fig. 9 of Shen et al., 2018). There was no SP2 available for the core-shell  
4 structure measurements in that study so it cannot really be proven that the observed  $\alpha_{abs}$  development  
5 was due to condensational growth even though it seems a good explanation and is qualitatively in line  
6 with Fig. 5.

7  
8  
9

### 10 **3.3 Unimodal size distributions with the same BC core fraction for all sizes**

11 The second approach is to assume that the BC core fraction – or equivalently the shell volume fraction  
12 – is the same for all sizes which means that the shell thickness increases with size as was visualized in  
13 Fig. 1b. This can be considered to be a result of aging of BC by not only condensational growth but also  
14 by cloud processing. The latter would lead to thick shells on particles activated into cloud droplets that  
15 would absorb for instance  $SO_2$  and  $NH_3$  and that would not rain but get later back into the aerosol phase  
16 by evaporation of cloud water. The constant volume fraction is not realistic but neither is the constant  
17 shell thickness. Both can be considered to be approximations.

18

19 In this approach the geometric standard deviations of the whole size distributions were set to  $\sigma_g = 1.4$ ,  
20 1.6 and 1.8 and the shell volume fractions to vary from 0% to 99%. The resulting  $\alpha_{abs}$  and BB(%) are  
21 presented as a function of  $D_g$ ,  $f_s$  and  $\sigma_g$  (Fig. 6). They are comparable with the analogous plots for single  
22 particles, i.e.,  $\sigma_g = 1.0$  (Fig. 2b, 2d, and 2f). **Note that from Eq. (2) it follows that the assumption of a**  
23 **constant  $f_s$  means that also the  $D_p$ -to- $D_{core}$  ratio  $R$  is constant and that the  $f_s$  range of 0 to 99%**  
24 **corresponds to the  $R$  range of 1 to 4.6. Figure 6 therefore has two y axes, one showing the  $f_s$  and the**  
25 **other the corresponding  $R$  values.**

26

27 Several observations can be made from Fig. 6. One of them is that the isoline of  $\alpha_{abs} = 1$  grows with  
28 growing  $D_g$  for each of the size distribution widths ( $\sigma_g$ ) but decreases with growing  $\sigma_g$ . Another is that  
29 the wider the size distribution is, the lower are the  $\alpha_{abs}$  and BB(%) at any given shell volume fraction.

1 The third one is that for all three widths  $\alpha_{abs}$  and BB(%) grows when  $f_s$  grows but that the growth is not  
2 uniformly distributed over the  $f_s$  vs.  $D_g$  space.

3

4 The last observation leads to calculations of size-dependent sensitivities of  $\alpha_{abs}$  to variations in  $f_s$ . The  
5 sensitivity was calculated as  $d\alpha_{abs}/df_s$  and its unit is  $\%^{-1}$ . Fig. 7a shows the sensitivities in the whole  $f_s$   
6 range of 1 - 99% as a function of  $D_g$  for the three size distribution widths. The sensitivity depends clearly  
7 on both  $D_g$  and  $\sigma_g$  of the size distribution and it also varies with  $f_s$ . It is very clear that  $\alpha_{abs}$  is most  
8 sensitive to  $f_s$  variations when  $D_g$  of the size distribution is in the accumulation mode sizes of 100 – 200  
9 nm. The sensitivity grows fairly steadily with growing  $f_s$  until for  $f_s > 90\%$  – which equals  $R > 2$  – it  
10 increases very strongly.

11

12 Another step for visualizing the sensitivities was taken by calculating size-dependent average  
13 sensitivities of  $\alpha_{abs}$  and BB(%) in three  $f_s$  ranges:  $f_s = 0 - 50\%$ ,  $50 - 90\%$  and  $90 - 99\%$  (Fig. 7b and 7c).

14 According to Eq. (2) the  $f_s$  ranges correspond to the R ranges of 1 – 1.3, 1.3 – 2.2 and 2.2 – 4.6. The lines  
15 in Fig. 7b and 7c These lines can be used for a rough estimate on a possible effect on  $\alpha_{abs}$  and BB(%).

16 For instance, if  $D_g \approx 140$  nm,  $\sigma_g = 1.4$ , and  $f_s \approx 50 - 90\%$ , an increase of  $f_s$  from 50% to 51% leads to an  
17  $\alpha_{abs}$  increase of  $\sim 0.01$  and consequently to a BB(%) increase of  $\sim 1\%$  when Aethalometer model  
18 constants of  $\alpha_{ff} = 0.9$ ,  $\alpha_{bb} = 1.68$  are used.

19

#### 20 **3.4 Bimodal size distributions with the same BC core fraction for all sizes in the mode**

21 Finally, bimodal size distributions are examined briefly. The size distributions consist of two externally  
22 mixed modes that have different shell volume fractions. In both modes the shell volume fractions are  
23 size-independent as in Fig. 1b. Mode 1 is an Aitken mode with the geometric mean diameter  $D_{g1}$  in the  
24 range 50 – 100 nm. There are two different settings for the Aitken mode: in the first case its number  
25 concentration is 10 times larger than that of the accumulation mode, i.e.,  $N_1 = 10N_2$ , it consists of almost  
26 pure fresh BC particles with  $f_{s1} = 5\%$  ( $R \approx 1.02$ ) and it is narrow,  $\sigma_{g1} = 1.4$ . In the second setting the  
27 number concentrations of the Aitken and accumulation mode are equal ( $N_1 = N_2$ ), the Aitken mode is  
28 aged so that  $f_{s1} = 50\%$  ( $R \approx 1.3$ ) and it is wider,  $\sigma_{g1} = 1.6$ . Mode 2 is an accumulation mode with the

1 geometric mean diameter  $D_{g2}$  in the range 100 – 500 nm,  $\sigma_{g2} = 1.6$  and it is very aged, with  $f_{s2} = 98\%$  (R  
2  $\approx 3.7$ ). The accumulation mode could be result of cloud processing as explained above.

3  
4 The results show that  $\alpha_{abs}$  is more sensitive to variations of the accumulation mode than of the Aitken  
5 mode (Fig. 8a). For instance, if  $D_{g2} < 250$  nm,  $\alpha_{abs} > 1$  at all  $D_{g1}$  values. Also, if  $D_{g1} = 60$  nm and  $D_{g2}$  varies  
6 in the whole range of 100 – 500 nm,  $\alpha_{abs}$  varies in the range of  $\sim 0.4 - 1.3$ . When the Aitken mode  
7 dominates the number concentration ( $N_1 = 10N_2$ ) with the fresh BC particles the maximum  $\alpha_{abs} \approx 1.2$  at  
8  $D_{g1} \approx 60$  nm and  $D_{g2} \approx 140$  nm is smaller than when the two modes have equal amount of particles. In  
9 the latter case the maximum  $\alpha_{abs} > 1.3$ . When the Aitken mode with  $f_s = 5\%$  dominates the number  
10 concentration the whole size distribution moves to the region that is less sensitive to  $f_s$  variations as  
11 discussed above in section 3.3. It is worth noting also that the maximum  $\alpha_{abs}$  and BB(%) values (Fig. 8b  
12 and 8c) are smaller than derived from the unimodal size distributions (section 3.3).

#### 13 14 4. Summary and conclusions

15 The purpose of this study is not to claim that all Aethalometer model results are wrong but that they  
16 have higher uncertainties than have been discussed in the literature. It is clear that there are BrC  
17 particles that have absorption Ångström exponents clearly larger than one, as shown in a very large  
18 number of publications. However, the size of light-absorbing particles and their coating even by purely  
19 scattering material affect clearly the wavelength dependence of absorption and thus have the potential  
20 to affect the Aethalometer model results. Since the wavelength dependency is used for source  
21 apportionment these effects have the potential to result in tens of percent too high or low contributions  
22 of wood-burning or fossil fuel emissions.

23  
24 There are some important results. In the modeling  $\alpha_{abs}$  equals 1 or 0.9  ~~$\alpha_{abs}$  equals 1~~ in very rare cases  
25 and thus BB(%) was very seldom 0% even though one type of BC was the only absorbing material in the  
26 simulations. The shape of size distribution plays an important role. Narrow size distributions result in  
27 higher  $\alpha_{abs}$  and BB(%) values than wide size distributions. The sensitivity of  $\alpha_{abs}$  and BB(%) to variations  
28 in shell volume fractions is the highest for accumulation mode particles. This is important because that  
29 is where the largest aerosol mass is.

1  
2 The goal of the paper was not to find out whether some pair of  $\alpha_{ff}$  and  $\alpha_{bb}$  is better than the other. Two  
3 well-known  $\alpha_{ff}$  and  $\alpha_{bb}$  pairs were used and shown how large the uncertainties may become just for  
4 these two pairs even if BC particles were coated by purely scattering material. The goal was not at all  
5 to find a good pair. On the contrary, the study shows that no constant values are good since in the real  
6 atmosphere BC particle size distributions are not constant, neither their mean diameter nor the coating  
7 of the particles. They all vary dynamically in the atmosphere. The study shows that any constant values  
8 will undoubtedly lead to large uncertainties of both the BB and FF fractions if no information on the  
9 size of the core or the thickness of the shell is available, even if purely scattering material is coating BC  
10 cores. As a conclusion, for the interpretation of absorption Ångström exponents it would be very  
11 important to measure BC size distributions and shell thicknesses together with the wavelength  
12 dependency of absorption.

13 ~~For the interpretation of absorption Ångström exponents it would be very good to measure BC size~~  
14 ~~distributions and shell thicknesses together with the wavelength dependency of absorption.~~

15  
16 There are obvious limitations in this study. A core-shell Mie model was used only so the work is limited  
17 to spherical particles. Fresh BC particles are usually agglomerates. There are studies that show that  
18 during aging processes these agglomerate may collapse and become closer to spherical particles so Mie  
19 modeling probably agrees better for aged than fresh BC particles. ~~And f~~Further, even if particles were  
20 spherical how well can they be modeled with a Mie code when they are collected on filters? Or does  
21 light absorption then follow the spectral absorbance of the bulk materials?

22  
23 This question could in principle be answered by generating spherical BC particles, coating them in an  
24 aging chamber with some non-absorbing material, for instance ammonium sulfate, and measuring both  
25 light absorption at multiple wavelengths with an Aethalometer and BC core size distributions and shell  
26 thicknesses with an SP2. If  $\alpha_{abs}$  increases ~~ed~~ up to some maximum value as a function of shell thickness  
27 and then starts ~~ed~~ decreasing like in the simulations above, then the process agrees with the growth of  
28 a size-independent coating. Or if  $\alpha_{abs}$  increases steadily then it suggests that the growth is size-

1 dependent and possibly with a size-independent shell volume fraction growth rate. If these are  
2 observed then the uncertainties discussed in this work should be taken seriously.

3  
4 On the other hand, if none of these effects were observed and the absorption Ångström exponents of  
5 the collected particles were  $\approx 1$  regardless of core size and shell thickness it would be safe to say that  
6 the Aethalometer measures the absorption spectra of the bulk materials and that the Aethalometer  
7 model yields correct results. Probably the truth is somewhere between these extremes: when the filter  
8 tape is still relatively clean the particles can be modeled even with a Mie code and for heavily-load  
9 filters  $\alpha_{\text{abs}}$  is that of bulk material. Also this could be tested experimentally.

10  
11 *Acknowledgements* This work was supported by the Academy of Finland via project NABCEA (grant  
12 no. 296302) and by Business Finland via project BC Footprint (grant nr. 528/31/2019)(~~grant no.~~  
13 ~~49402-201040~~).

#### 14 15 **References**

16 Andreae, A. and Gelencser, A.: Black carbon or brown carbon? The nature of light-absorbing  
17 carbonaceous aerosols, *Atmos. Chem. Phys.*, 6, 3131–3148, [http://www.atmos-chem-](http://www.atmos-chem-phys.net/6/3131/2006)  
18 [phys.net/6/3131/2006](http://www.atmos-chem-phys.net/6/3131/2006), 2006.

19  
20 Arola, A., Schuster, G., Myhre, G., Kazadzis, S., Dey, S., and Tripathi, S. N.: Inferring absorbing organic  
21 carbon content from AERONET data, *Atmos. Chem. Phys.*, 11, 215–225, [https://doi.org/10.5194/acp-](https://doi.org/10.5194/acp-11-215-2011)  
22 [11-215-2011](https://doi.org/10.5194/acp-11-215-2011), 2011.

23  
24 Bergstrom, R.W., Pilewskie, P., Russell, P. B., Redemann, J., Bond, T., Quinn, P. K., and Sierau, B.: Spectral  
25 Absorption Properties of Atmospheric Aerosols, *Atmos. Chem. Phys.*, 7, 5937–5943,  
26 <http://www.atmos-chem-phys.net/7/5937/2007>, 2007.

27  
28 Bond, T. C. and Bergstrom, R. W.: Light Absorption by Carbonaceous Particles: An Investigative  
29 Review, *Aerosol Sci. Technol.*, 40, 27–67, 2006.

1  
2 Bond, T. C., Doherty, S. J., Fahey, D. W., Forster, P. M., Berntsen, T., DeAngelo, B. J., Flanner, M. G.,  
3 Ghan, S., Kärcher, B., Koch, D., Kinne, S., Kondo, Y., Quinn, P. K., Sarofim, M. C., Schultz, M.  
4 G., Schulz, M., Venkataraman, C., Zhang, H., Zhang, S., Bellouin, N., Guttikunda, S. K., Hopke, P. K.,  
5 Jacobson, M. Z., Kaiser, J. W., Klimont, Z., Lohmann, U., Schwarz, J. P., Shindell, D., Storelvmo, T.,  
6 Warren, S. G., and Zender, C.S.: Bounding the role of black carbon in the climate system: A scientific  
7 assessment, *J. Geophys. Res. Atmos.*, **118**, 2013.  
8  
9 Cazorla, A., Bahadur, R., Suski, K. J., Cahill, J. F., Chand, D., Schmid, B., Ramanathan, V., and Prather, K.  
10 A.: Relating aerosol absorption due to soot, organic carbon, and dust to emission sources determined  
11 from in-situ chemical measurements, *Atmos. Chem. Phys.*, **13**, 9337–9350,  
12 <https://doi.org/10.5194/acp-13-9337-2013>, 2013.  
13  
14 [Chung, C., Ramanathan, V., and Decremier, D.: Observationally constrained estimates of carbonaceous](#)  
15 [aerosol radiative forcing, \*P. Natl. Acad. Sci. USA\*, \*\*109\*\*, 11624–11629, 2012.](#)  
16  
17 Chylek, P., Lee, J. E., Romonosky, D. E., Gallo, F., Lou, S., Shrivastava, M., et al.: Mie scattering captures  
18 observed optical properties of ambient biomass burning plumes assuming uniform black, brown, and  
19 organic carbon mixtures. *J. Geophys. Res., Atmospheres*, **124**, 11406–11427.  
20 <https://doi.org/10.1029/2019JD031224>, 2019.  
21  
22 Devi, J.J., Bergin, M., McKenzie, M., Schauer, J.J., and Weber, R.: Contribution of particulate brown  
23 carbon to light absorption in the rural and urban Southeast US, *Atmos. Environ.*, **136**, 95 - 104, 2016.  
24  
25 Feng, Y., Ramanathan, V., and Kotamarthi, V. R.: Brown carbon: a significant atmospheric absorber of  
26 solar radiation?, *Atmos. Chem. Phys.*, **13**, 8607–8621, <https://doi.org/10.5194/acp-13-8607-2013>,  
27 2013.  
28

1 Fuller, G.W., Tremper, A.H., Baker, T.D., Yttri, K.E., Butterfield, D.: Contribution of wood burning to  
2 PM10 in London. *Atmos. Environ.* 87, 87–94, 2014.

3

4 Gyawali, M., Arnott, W. P., Lewis, K., and Moosmüller, H.: In situ aerosol optics in Reno, NV, USA during  
5 and after the summer 2008 California wildfires and the influence of absorbing and non-absorbing  
6 organic coatings on spectral light absorption, *Atmos. Chem. Phys.*, 9, 8007-8015, doi:10.5194/acp-9-  
7 8007-2009, 2009.

8

9 Harrison, R.M., Beddows, D.C., Jones, A.M., Calvo, A., Alves, C., Pio, C.: An evaluation of some issues  
10 regarding the use of aethalometers to measure woodsmoke concentrations. *Atmos. Environ.* 80, 540–  
11 548, 2013.

12

13 Healy, R., Sofowote, U., Su, Y., Deboz, J., Noble, M., Jeong, C.-H., Wang, J., Hilker, N., Evans, G.,  
14 Doerksen, G.: Ambient measurements and source apportionment of fossil fuel and biomass burning  
15 black carbon in Ontario. *Atmos. Environ.* 161, 34–47, 2017.

16

17 Helin, A., Niemi, J., Virkkula, A., Pirjola, L., Teinilä, K., Backman, J., Aurela, M., Saarikoski, S., Rönkkö, T.,  
18 Asmi, E., Timonen, H.: Characteristics and source apportionment of black carbon in the Helsinki  
19 metropolitan area, Finland, *Atmos. Environ.*, 190, 87 – 98, doi: 10.1016/j.atmosenv.2018.07.022, 2018.

20

21 Herich, H., Hueglin, C., and Buchmann, B.: A 2.5 year’s source apportionment study of black carbon  
22 from wood burning and fossil fuel combustion at urban and rural sites in Switzerland, *Atmos. Meas.*  
23 *Tech.*, 4, 1409–1420, doi:10.5194/amt-4-1409-2011, 2011.

24

25 Kirchstetter, T. W., Novakov, T., and Hobbs, P. V.: Evidence that the spectral dependence of  
26 light absorption by aerosols is affected by organic carbon, *J. Geophys. Res.*, 109, D21208,  
27 doi:10.1029/2004JD004999, 2004.

28



1 Kirchstetter, T. W. and Thatcher, T. L.: Contribution of organic carbon to wood smoke particulate matter  
2 absorption of solar radiation, *Atmos. Chem. Phys.*, 12, 6067–6072, doi:10.5194/acp-12-6067-2012,  
3 2012.  
4

5 Kondo, Y., L. Sahu, N. Moteki, F. Khan, N. Takegawa, X. Liu, M. Koike, and T. Miyakawa: Consistency and  
6 traceability of black carbon measurements made by laser-induced incandescence, thermal-optical  
7 transmittance, and filter-based photo-absorption techniques, *Aerosol Sci. Technol.*, 45, 295–312,  
8 doi:10.1080/02786826.2010.533215, 2011.  
9

10 Lack, D. A. and Cappa, C. D.: Impact of brown and clear carbon on light absorption enhancement,  
11 single scatter albedo and absorption wavelength dependence of black carbon, *Atmos. Chem. Phys.*,  
12 10, 4207–4220, doi:10.5194/acp-10-4207-2010, 2010.  
13

14 Lack, D. A. and Langridge, J. M.: On the attribution of black and brown carbon light absorption using  
15 the Ångström exponent, *Atmos. Chem. Phys.*, 13, 10535–10543, [https://doi.org/10.5194/acp-13-](https://doi.org/10.5194/acp-13-10535-2013)  
16 10535-2013, 2013.  
17

18 Lack, D. A., Langridge, J. M., Bahreini, R., Cappa, C. D., Middlebrook, A. M., and Schwarz, J. P.: Brown  
19 carbon and internal mixing in biomass burning particles, *P. Natl. Acad. Sci. USA*, 109, 14802–14807,  
20 2012.  
21

22 Laskin, A., Laskin, J., and Nizkorodov, S. A.: Chemistry of Atmospheric Brown Carbon, *Chem.*  
23 *Rev.*, 115, 4335–4382, <https://doi.org/10.1021/cr5006167>, 2015.  
24

25 Liu, C., Chung, C. E., Yin, Y., and Schnaiter, M.: The absorption Ångström exponent of black carbon:  
26 from numerical aspects, *Atmos. Chem. Phys.*, 18, 6259–6273, [https://doi.org/10.5194/acp-18-6259-](https://doi.org/10.5194/acp-18-6259-2018)  
27 2018, 2018.  
28

1 Moosmüller, H., Chakrabarty, R. K., Ehlers, K. M., and Arnott, W. P.: Absorption Ångström coefficient,  
2 brown carbon, and aerosols: basic concepts, bulk matter, and spherical particles, *Atmos. Chem. Phys.*,  
3 **11**, 1217–1225, doi:10.5194/acp-11-1217-2011, 2011.

4

5 Moteki, N., Y. Kondo, Y. Miyazaki, N. Takegawa, Y. Komazaki, G. Kurata, T. Shirai, D. R. Blake, T.  
6 Miyakawa, and Koike, M.: Evolution of mixing state of black carbon particles: Aircraft measurements  
7 over the western Pacific in March 2004, *Geophys. Res. Lett.*, **34**, L11803, doi:10.1029/2006GL028943,  
8 2007.

9

10 Russell, P., Bergstrom, R., Shinozuka, Y., Clarke, A., Decarlo, P., Jimenez, J., Livingston, J., Redemann,  
11 J., Dubovik, O., and Strawa, A.: Absorption Angstrom Exponent in AERONET and related data as an  
12 indicator of aerosol composition, *Atmos. Chem. Phys.*, **10**, 1155–1169, 2010.

13

14 Saleh, R., Hennigan, C., McMeeking, G., Chuang, W., Robinson, E., Coe, H., Donahue, N., Robinson, A.:  
15 Absorptivity of brown carbon in fresh and photo-chemically aged biomass-burning emissions. *Atmos.*  
16 *Chem. Phys.* **13**, 7683–7693, 2013.

17

18 Sandradewi, J., Prevot, A. S. H., Szidat, S., Perron, N., Alfarra, M. R., Lanz, V. A., Weingartner, E., and  
19 Baltensperger, U.: Using aerosol light absorption measurements for the quantitative determination of  
20 wood burning and traffic emission contributions to particulate matter, *Environ. Sci. Technol.*, **42**, 3316–  
21 3323, 2008a.

22

23 Sandradewi, J., Prevot, A. S. H., Weingartner, E., Schmidhauser, R., Gysel, M., and Baltensperger, U.:  
24 A study of wood burning and traffic aerosols in an Alpine valley using a multi-wavelength Aethalometer,  
25 *Atmos. Environ.*, **42**, 101–112, 2008b.

26

27 [Schuster, G. L., Dubovik, O., Arola, A., Eck, T. F., and Holben, B. N.: Remote sensing of soot carbon – Part](https://doi.org/10.5194/acp-16-1587-2016)  
28 [2: Understanding the absorption Ångström exponent, \*Atmos. Chem. Phys.\*, \*\*16\*\*, 1587–1602,](https://doi.org/10.5194/acp-16-1587-2016)  
29 <https://doi.org/10.5194/acp-16-1587-2016>.

1  
2 Schwarz, J. P., Gao, R. S., Spackman, J. R., Watts, L. A., Thomson, D. S., Fahey, D. W., Ryerson, T. B.,  
3 Peischl, J., Holloway, J. S., Trainer, M., Frost, G. J., Baynard, T., Lack, D. A., de Gouw, J. A., Warneke,  
4 C., and Del Negro, L. A.: Measurement of the mixing state, mass, and optical size of individual black  
5 carbon particles in urban and biomass burning emissions, *Geophys. Res. Lett.*, 35, L13810,  
6 doi:10.1029/2008GL033968, 2008.

7  
8 Shen, Y., Virkkula, A., Ding, A., Wang, J., Chi, X., Nie, W., Qi, X., Huang, X., Liu, Q., Zheng, L., Xu, Z., Petäjä,  
9 T., Aalto, P. P., Fu, C., and Kulmala, M.: Aerosol optical properties at SORPES in Nanjing, east China,  
10 *Atmos. Chem. Phys.*, 18, 5265–5292, <https://doi.org/10.5194/acp-18-5265-2018>, 2018.

11  
12 Shiraiwa, M., Y. Kondo, N. Moteki, N. Takegawa, L. K. Sahu, A. Takami, S. Hatakeyama, S. Yonemura,  
13 and D. R. Blake: Radiative impact of mixing state of black carbon aerosol in Asian outflow, *J. Geophys.*  
14 *Res.*, 113, D24210, doi:10.1029/2008JD010546, 2008.

15  
16 Valenzuela, A., Olmo, F.J., Lyamani, H., Antón, M., Titos, G., Cazorla, A., Alados-Arboledas, L.: Aerosol  
17 scattering and absorption Angström exponents as indicators of dust and dust-free days over Granada  
18 (Spain). *Atmos Res.*, 154, pp. 1-13. 2015.

19  
20 Wang, X., Heald, C. L., Sedlacek, A. J., de Sá, S. S., Martin, S. T., Alexander, M. L., Watson, T. B., Aiken,  
21 A. C., Springston, S. R., and Artaxo, P.: Deriving brown carbon from multiwavelength absorption  
22 measurements: method and application to AERONET and Aethalometer observations, *Atmos.*  
23 *Chem. Phys.*, 16, 12733–12752, <https://doi.org/10.5194/acp-16-12733-2016>, 2016.

24  
25 Wu Z.P., Wang Y.P.: Electromagnetic scattering for multilayered spheres: recursive algorithms, *Radio*  
26 *Science*, 26, 1393-1401, 1991.

27

1 Zhang, X., Mao, M., Yin, Y., and Tang, S.: The absorption Ångstrom exponent of black carbon with brown  
2 coatings: effects of aerosol microphysics and parameterization, *Atmos. Chem. Phys.*, 20, 9701–9711,  
3 <https://doi.org/10.5194/acp-20-9701-2020>, 2020.

4

5 Zotter, P., Herich, H., Gysel, M., El-Haddad, I., Zhang, Y., Močnik, G., Hüglin, C., Baltensperger, U., Szidat,  
6 S., and Prévôt, A. S. H.: Evaluation of the absorption Ångström exponents for traffic and wood burning  
7 in the Aethalometer-based source apportionment using radiocarbon measurements of ambient  
8 aerosol, *Atmos. Chem. Phys.*, 17, 4229–4249, <https://doi.org/10.5194/acp-17-4229-2017>, 2017.

9

1 **Tables**

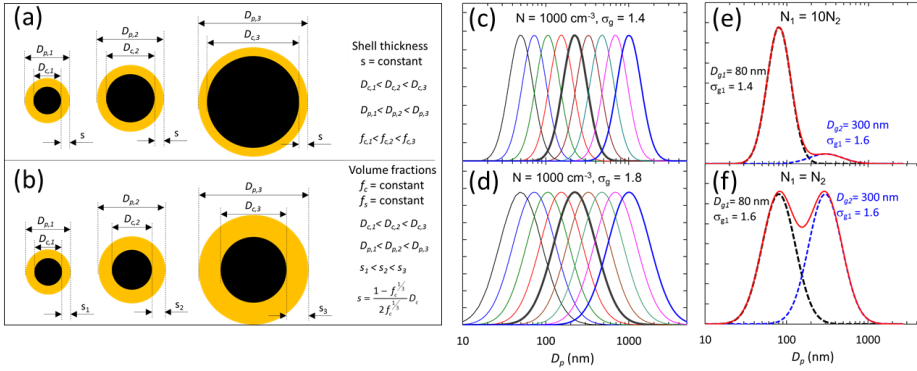
2

3 **Table 1. Nomenclature**

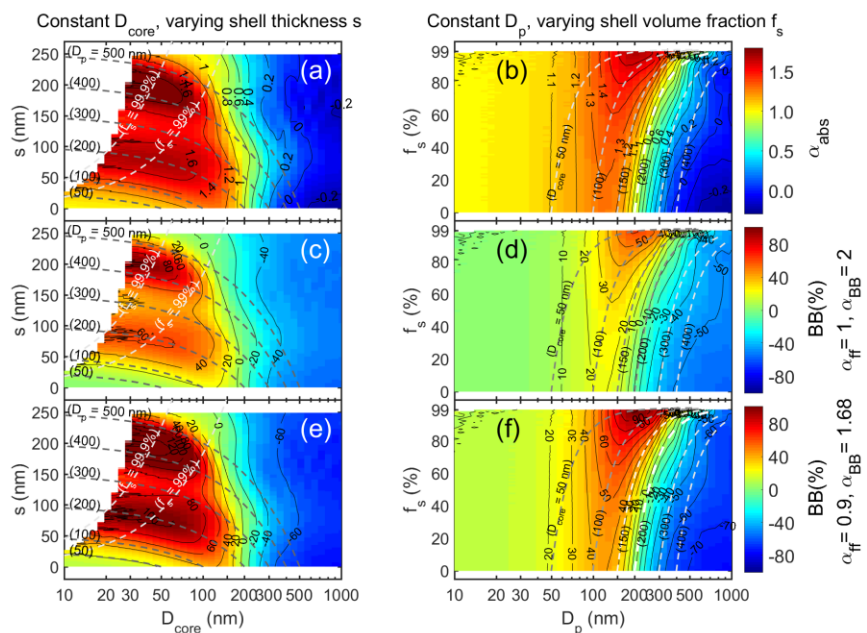
Symbol	Definition	Unit	Equation
$D_p$	Particle diameter	nm	(1)
$D_{core}$	Diameter of the BC core particle	nm	(1)
$D_g$	Geometric mean diameter of a size distribution	nm	
$D_{g,core}$	Geometric mean diameter of the BC core size distribution	nm	
$D_{g1}$	$D_g$ of the first mode of a bimodal size distribution	nm	
$D_{g2}$	$D_g$ of the second mode of a bimodal size distribution	nm	
$\sigma_g$	Geometric standard deviation of a size distribution	-	
$\sigma_{g,core}$	Geometric standard deviation of the BC core size distribution	-	
$\sigma_{g1}$	$\sigma_g$ of the first mode of a bimodal size distribution	-	
$\sigma_{g2}$	$\sigma_g$ of the second mode of a bimodal size distribution	-	
$n(D_p, D_g, \sigma_g)$	Lognormal particle number size distribution	$cm^{-3}$	
$N_1$	Number concentration of the first mode of a bimodal size distribution	$cm^{-3}$	
$N_2$	Number concentration of the second mode of a bimodal size distribution	$cm^{-3}$	
$N_i$	Number concentration of particle size $D_{p,i}$	$cm^{-3}$	(3)
$V_p$	Particle volume	$m^3$	(1)
$V_{core}$	Volume of the BC core	$m^3$	(1)
$f_c$	Core volume fraction	-	(1)
$f_s$	Shell volume fraction	-	
$s$	Shell thickness	nm	(1)
$R$	Ratio of the particle diameter to the BC core diameter ( $D_p$ -to- $D_{core}$ ratio)	-	(2)
$R_{N(D_p)}$	Number-weighted $D_p$ -to- $D_{core}$ ratio	-	(3)
$R_i$	$D_p$ -to- $D_{core}$ ratio of the particle diameter $D_{p,i}$	-	(3)
$\sigma_{ap}(\lambda)$	Absorption coefficient at the wavelength $\lambda$	$Mm^{-1}$	(4)
$\sigma_{ap,bb}(\lambda)$	Absorption coefficient of particles from biomass burning at the wavelength $\lambda$	$Mm^{-1}$	(6)
$Q_a$	Absorption efficiency	-	(4)
$m_{core}$	Complex refractive index of the BC core	-	(4)
$m_{shell}$	Complex refractive index of the shell	-	(4)
$\alpha_{abs}$	Absorption Ångström exponent	-	
$\alpha_{abs}(\lambda_1/\lambda_2)$	Absorption Ångström exponent for the wavelength pair $\lambda_1, \lambda_2$	-	(5)
$\alpha_{ff}$	$\alpha_{abs}$ of fossil fuel BC in the Aethalometer model	-	(6)
$\alpha_{bb}$	$\alpha_{abs}$ of biomass-burning BC in the Aethalometer model	-	(6)

4

1 **Figures**



2  
 3 Figure 1. Examples of particles and size distributions used in the simulations: a) particles with a BC core  
 4 coated with a constant shell thickness  $s$ , b) particles with constant BC core and shell volume fractions  $f_c$   
 5 and  $f_s$ , c) unimodal narrow size distributions with the geometric standard deviation of  $\sigma_g = 1.4$ , d)  
 6 unimodal wide size distributions with  $\sigma_g = 1.8$ , e) bimodal size distributions with a dominating Aitken  
 7 mode, f) bimodal size distributions with equal-sized Aitken and accumulation modes.  
 8

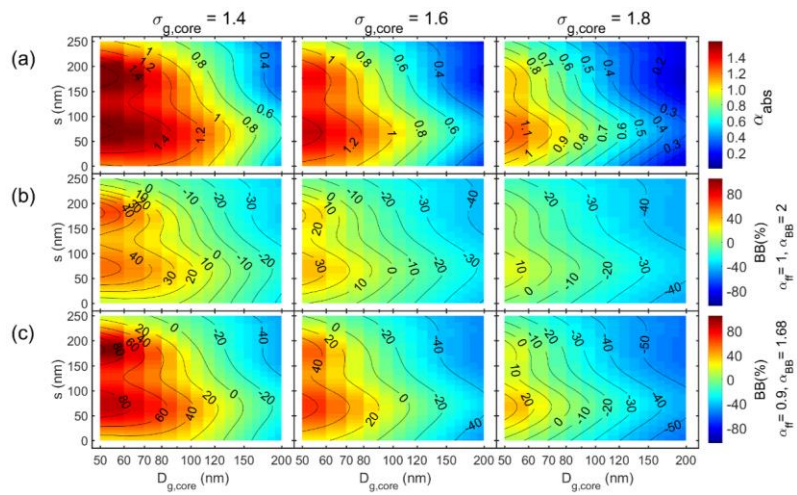


1

2 Figure 2. Absorption Ångström exponent ( $\alpha_{abs}$ ) and the from it calculated fraction of biomass-burning  
 3 BC for single coated particles as a function of (in -a, c, and e) BC core diameter ( $D_{core}$ ) and shell thickness  
 4 ( $s$ ) and (b, d, and f) as a function of particle diameter ( $D_p = D_{core} + 2s$ ) and shell volume fraction  $f_s$  in the  
 5 range  $f_s \leq 99\%$ . In a), c) and e) the dark dashed lines show the  $D_{core}$  and  $s$  of particles that have the  
 6 same  $D_p$  – written in parentheses – at all shell thicknesses and the light dashed line show the shell  
 7 thicknesses that correspond to  $f_s = 99\%$  and  $99.9\%$ . In b), d) and f) the dashed lines show the  $D_p$  and  $f_s$   
 8 of particles that have the same  $D_{core}$  – written in parentheses – at all shell volume fractions. The color  
 9 bars are common for a and b, c and d, and e and f.

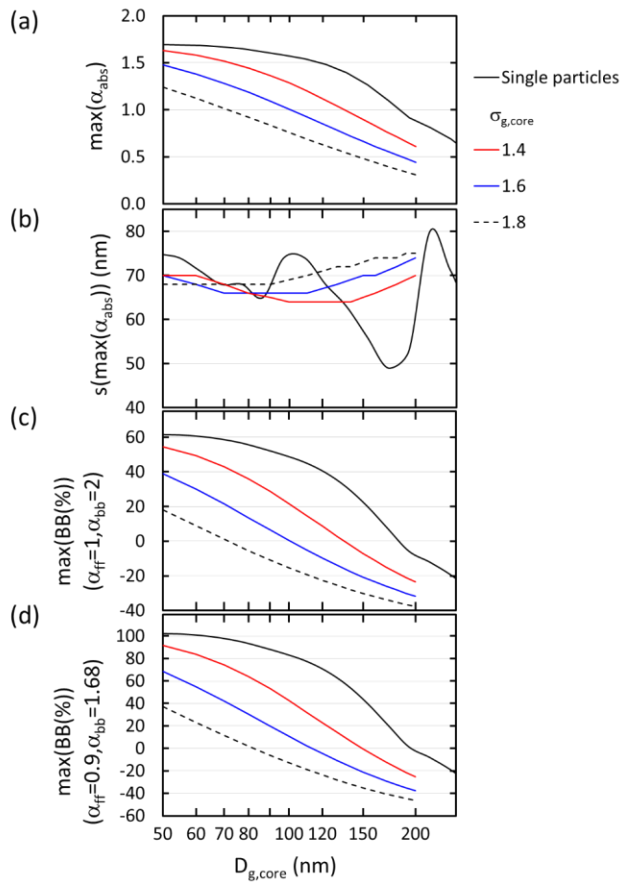
10

11



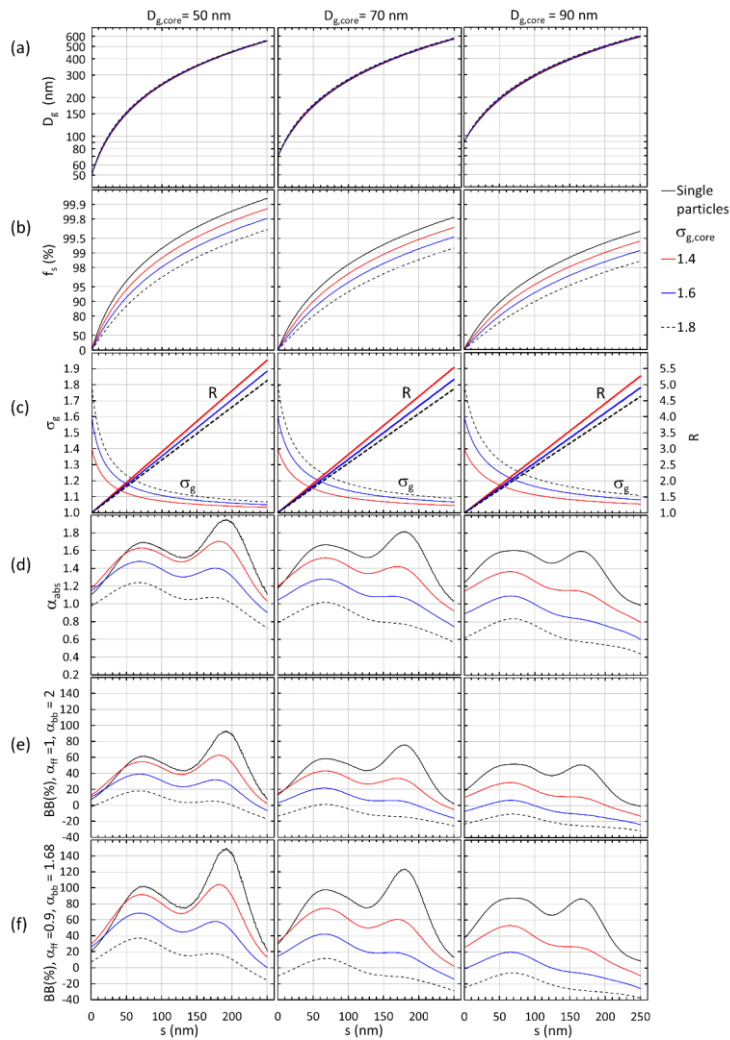
1  
 2 Figure 3. Unimodal particle size distributions with a size-independent shell thickness ( $s$ ) for three widths  
 3 of the core size distributions:  $\sigma_{g,core} = 1.4, 1.6$  and  $1.8$ . a) absorption Ångström exponent ( $\alpha_{abs}$ ) and the  
 4 from it calculated fraction of biomass-burning BC (BB(%)) with the Aethalometer model constants of b)  
 5  $\alpha_{ff} = 1, \alpha_{bb} = 2$  and c)  $\alpha_{ff} = 0.9, \alpha_{bb} = 1.68$  vs. the geometric mean diameter of the core ( $D_{g,core}$ ).





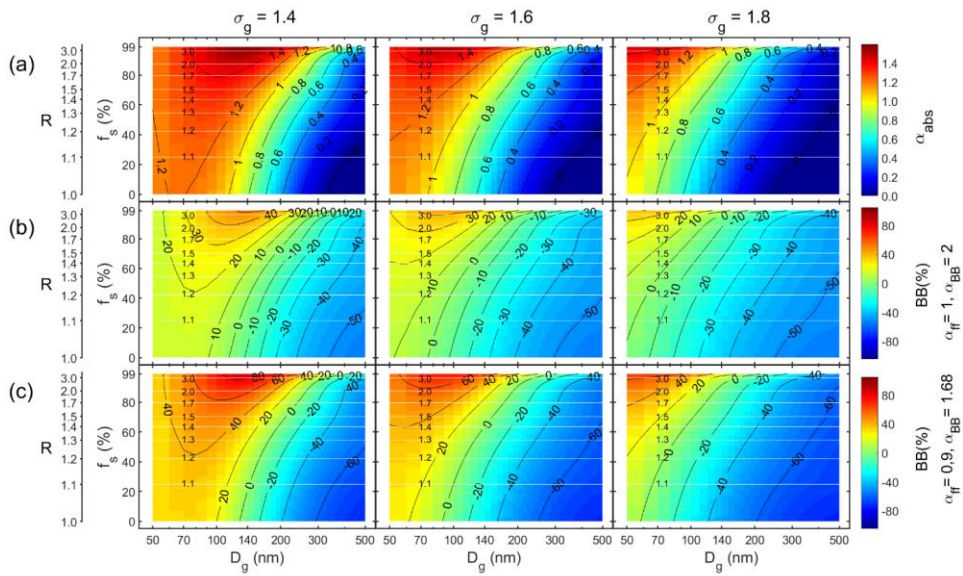
1  
2 Figure 4. Size distribution dependence of the first maximum of  $\alpha_{abs}$  when a size-independent shell grows  
3 on a BC core: a) the first maximum value of  $\alpha_{abs}$ , b) the shell thickness at the maximum  $\alpha_{abs}$ , c) maximum  
4 biomass-burning fraction with the Aethalometer model constants  $\alpha_{ff} = 1$  and  $\alpha_{bb} = 2$ , and d) maximum  
5 biomass-burning fraction with the Aethalometer model constants  $\alpha_{ff} = 0.9$  and  $\alpha_{bb} = 1.68$  as a function  
6 of the geometric mean diameter ( $D_{g,core}$ ) and the geometric standard deviation ( $\sigma_{g,core}$ ) of the BC core.

7  
8  
9

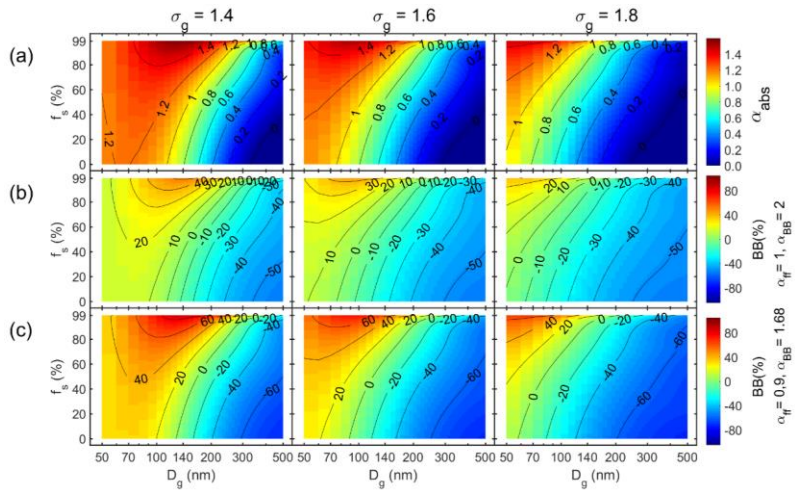


1  
 2 **Figure 5.** Examples of the growth of a non-size-dependent scattering shell on BC core size distributions with  $D_{g,core} = 50$  nm,  
 3 70 nm and 90 nm **and on single BC particles**. a) Geometric mean diameter, b) shell volume fraction, c) geometric standard  
 4 deviation and  $D_p$ -to- $D_{core}$  ratio (R), d) absorption Ångström exponent, e) BB(%) with the Aethalometer model constants  $\alpha_{HF} =$   
 5 1 and  $\alpha_{BB} = 2$ , and d) biomass-burning fraction with the Aethalometer model constants  $\alpha_{HF} = 0.9$  and  $\alpha_{BB} = 1.68$  as a function  
 6 shell thickness  $s$ .

Formatted: Font: 10 pt  
 Formatted: Font: 10 pt  
 Formatted: Font: 10 pt  
 Formatted: Font: 10 pt  
 Formatted: Font: 10 pt  
 Formatted: Font: 10 pt  
 Formatted: Font: 10 pt  
 Formatted: Font: 10 pt  
 Formatted: Font: 10 pt  
 Formatted: Font: 10 pt



1



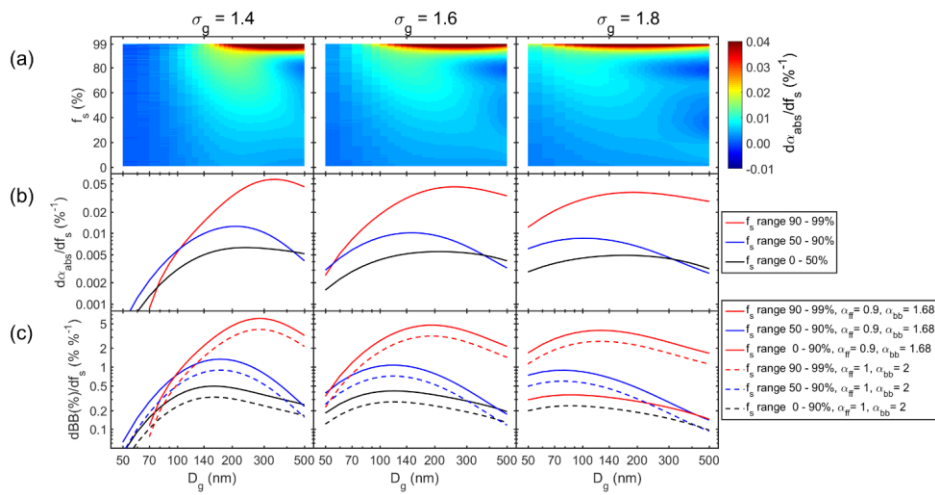
2

3 Figure 6. Unimodal particle size distributions with size-independent shell volume fractions  $f_s$  and three  
 4 widths of the size distributions:  $\sigma_g = 1.4, 1.6$  and  $1.8$ . a) absorption Ångström exponent ( $\alpha_{abs}$ ) and the  
 5 from it calculated fraction of biomass-burning BC (BB(%)) with the Aethalometer model constants of b)

1  $\alpha_{ff} = 1$ ,  $\alpha_{bb} = 2$  and c)  $\alpha_{ff} = 0.9$ ,  $\alpha_{bb} = 1.68$  vs. the geometric mean diameter of the whole size distribution

2 ( $D_g$ ). The white horizontal grid lines show constant  $D_p$ -to- $D_{core}$  ratios (= R).

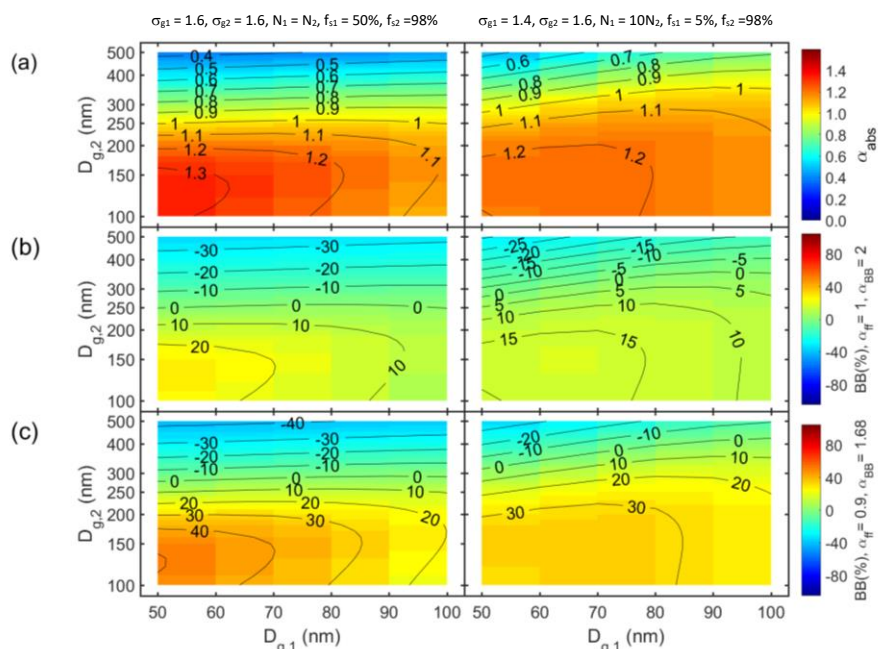
3



1  
 2 Figure 7. Size-dependent sensitivity of  $\alpha_{abs}$  and BB(%) to variations of the shell volume fraction  $f_s$ . a)  $\alpha_{abs}$   
 3 sensitivity in the whole  $f_s$  range of 1 - 99%, b) average  $\alpha_{abs}$  sensitivity in three  $f_s$  ranges, and (c) average  
 4 BB(%) sensitivities in three  $f_s$  ranges.

5  
 6

1



2

3 Figure 8. Bimodal particle size distributions with size-independent shell volume fractions  $f_s$  in two  
 4 modes as a function of geometric mean diameters of mode 1 ( $D_{g1}$ ) and mode 2 ( $D_{g2}$ ). a) absorption  
 5 Ångström exponent ( $\alpha_{abs}$ ) and the from it calculated fraction of biomass-burning BC (BB(%)) with the  
 6 Aethalometer model constants of b)  $\alpha_{ff} = 1$ ,  $\alpha_{bb} = 2$  and c)  $\alpha_{ff} = 0.9$ ,  $\alpha_{bb} = 1.68$ . The widths, the relative  
 7 number of particles in the two modes and the shell volume fractions of the two modes on the left  
 8 column:  $\sigma_{g1} = 1.6$ ,  $\sigma_{g2} = 1.6$ ,  $N_1 = N_2$ ,  $f_{s1} = 50\%$ ,  $f_{s2} = 98\%$  and on the right column:  $\sigma_{g1} = 1.4$ ,  $\sigma_{g2} = 1.6$ ,  $N_1$   
 9  $= 10N_2$ ,  $f_{s1} = 5\%$ ,  $f_{s2} = 98\%$ .